

Automatically detecting rotation in chest radiographs using principal rib-orientation measure for quality control

K. C. Santosh[†], S. Candemir, S. Jaeger, A. Karargyris, S. Antani, G. Thoma

National Library of Medicine, National Institutes of Health

8600 Rockville Pike, Bethesda, MD 20894, USA

L. Folio

Department of Radiology and Imaging Sciences, Clinical Center, National Institutes of Health

8600 Rockville Pike, Bethesda, MD 20892, USA

Email: {santosh.kc, sema.candemir, stefan.jaeger, alex.Karargyris, les.folio, sameer.antani, george.thoma}@nih.gov

[†]Corresponding author

Abstract. We present a novel method for detecting rotated lungs in chest radiographs for quality control and augmenting automated abnormality detection. The method computes a principal rib-orientation measure using a generalized line histogram technique for quality control, and therefore augmenting automated abnormality detection. To compute the line histogram, we use line seed filters as kernels to convolve with edge images, and extract a set of lines from the posterior rib-cage. After convolving kernels in all possible orientations in the range $[0^\circ, 180^\circ)$, we measure the angle with maximum magnitude in the line histogram. This measure provides an approximation of the principal chest rib-orientation for each lung. A chest radiograph is upright if the difference between the orientation angles of both lungs with respect to the horizontal axis is negligible. We validate our method on sets of normal and abnormal images and argue that rib orientation can be used for rotation detection in chest radiographs as an aid in quality control during image acquisition. It can also be used for training and testing data sets for computer aided diagnosis research, for example. In our experiments, we achieve a maximum accuracy of approximately 90%.

Keywords. Chest radiographs · Automation · Pattern recognition · Quality control · Generalized line histogram · Rib-orientation · Rotation detection.

1. Introduction

1.1 Motivation

Automated quality control is a critical issue when large number of digital chest radiographs (CXR) need to be acquired, such as during mass population automated screening [Jaeger et al. \(2014\)](#). During image acquisition, CXRs need to be assessed for proper x-ray penetration, adequate inspiration (inhaling) by the patient, proper angulation, and importantly, the image should be devoid of any rotation [Corne & Pointon \(2010\)](#); [Puddy & Hill \(2007\)](#). Problems with any of these can hinder the interpretive process. Unless the technical quality is checked carefully, the CXR film may be misinterpreted (misread) [Corne & Pointon \(2010\)](#); [Herring \(2011\)](#). Among these, rotation, in particular, can adversely affect the performance of subsequent automated processing steps in screening algorithms or computer-aided diagnosis, such as lung segmentation [Iakovidis et al. \(2009\)](#) and lateral one-to-one zone comparison, viz. upper, middle, and lower between lung sections. In case of zone comparison, zone splitting horizontal lines (with respect to x-axis that goes in accordance with the x-ray beam) may not equally crop zones from both lung sections when the CXR is rotated.

While rotated chest radiographs may not necessarily be challenging for radiologists [Folio \(2012; 2014\)](#), machines that are operated in either a computer-assisted or a fully-automated fashion, may not be capable of accurately processing rotated films (CXRs). An automatic method for detecting rotated images is desirable to enable machines to detect a rotated CXR and alert a human operator for closer inspection. Therefore, detecting rotation in chest radiographs is the core theme of the paper. Since our focus is on quality control, we try to detect all rotated radiographs that could cause problems for our automated screening system [Jaeger et al. \(2014\)](#). This includes radiographs displaying diseases, such as scoliosis, or spinal fixations and other surgery resulting in anatomic deformity that is not typically considered as rotation from the radiologist point of view. In addition, most individuals have some degree of lateral curvature of the spine, giving the appearance of a minor rotation. We also do not distinguish between rotation along a single axis and multiple axes [Folio \(2010\)](#). Most rotations involve multiple axes and pose harder problems for automatic processing than rotations involving only one axis, but most of them pose no major reading problems for radiologists.

1.2 Context and our contribution

Rotation in CXRs is likely to occur in images acquired with portable machines in non-hospital settings or under more challenging outdoor conditions, such as mobile screening stations in rural areas. In addition to pathology-related rotations, misaligned body positions are more frequent in these cases due to hardware limitations of the screening setup used, poorly-observed screening protocols, or other factors caused by mass population screening stress [Bongard et al. \(2008\)](#); [Jaeger et al. \(2013\)](#). To acquire an upright CXR, a radiology technician needs to align the patient's body (upper part of the body, more specifically) so that it is perpendicular to

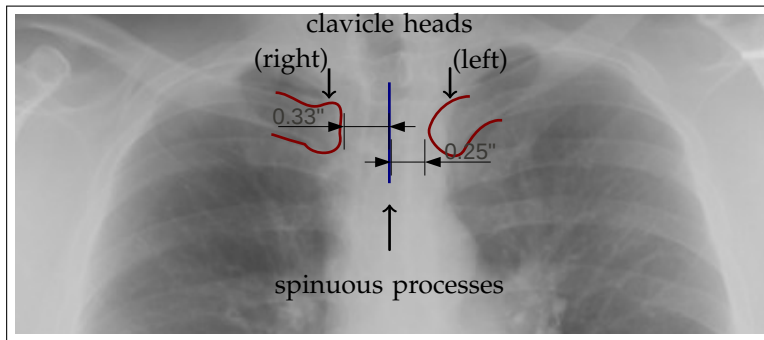


Fig. 1. A graphical illustration (cropped CXR) of one method radiologists estimate rotation in chest radiographs [Corne & Pointon \(2010\)](#); [Herring \(2011\)](#).

the x-ray beam (principal axis). Deviation from this position often results in a rotated CXR. The degree of rotation in a CXR can be computed by analyzing the relationship of the medial heads of the clavicles to adjacent appearing vertebral spinous processes in the upper thorax region [Folio \(2012\)](#). Normally, the spinous processes lie equidistant from the medial heads of the clavicles [Corne & Pointon \(2010\)](#); [Puddy & Hill \(2007\)](#) (see Fig. 1). If one clavicle is nearer than the other then the CXR is rotated and the lung on that side will appear whiter [Corne & Pointon \(2010\)](#); [Herring \(2011\)](#). Therefore, it is necessary to first detect the clavicles and the adjacent vertebra in the spinous processes, and then compute the distance between them. From a practical point of view, the automatic detection of clavicle heads and spinous processes needs to be precise since a small deviation with respect to the actual boundary can adversely affect the decision process. When compared with human performance, automatic state-of-the-art methods do not provide satisfactory clavicle boundary detection performance due to the large variation in intensity distributions in the clavicle region, the presence of shadows, and other pathology such as nodules [Horváth et al. \(2009\)](#); [van Ginneken et al. \(2006\)](#). Therefore, [Suzuki et al. \(2006\)](#) recommend that the automatic systems be trained on large datasets.

In contrast, when clavicles do not provide necessary information, we observe that radiologists can reliably determine if a CXR is rotated by using other contextual information, e.g. patient details. While there are instances where the spinous process and clavicles are discordant with rib rotation, we assume in the following that a rotated lung affects the positions of clavicles and ribs in a consistent way for the vast majority of cases (see Fig. 2). Motivated by this, we determine rotation in chest radiographs based on the rib-orientation. Computing the rib-vertebra angle i.e., the angle between a rib and its corresponding vertebra is not a new concept and it has been a clinically accepted method since the 1970's [Grivas et al. \(1992\)](#); [Mehta \(1972\)](#). These works used radiographs of scoliosis patients for which they computed the rib-vertebra angle difference (RVAD) from all ribs to examine the influence of the infantile growth spurt and to stress the importance of early diagnosis and treatment. Similarly, interval change detection between two CXRs based on the difference in anterior-posterior inclination angles has been reported as an image registration method [Matsuo et al. \(2005\)](#). As with clavicle detection performance, low accuracy in rib detection has been reported in [de Souza \(1983\)](#); [Karargyris et al. \(2011\)](#); [Suzuki et al. \(2006\)](#); [Wechsler \(1977\)](#). This means that an automated method should not rely on a complete rib cage detection as not all 12 pairs of ribs (including false and floating ribs) are necessarily visible in a typical radiograph. The latter issue can be considered as the major

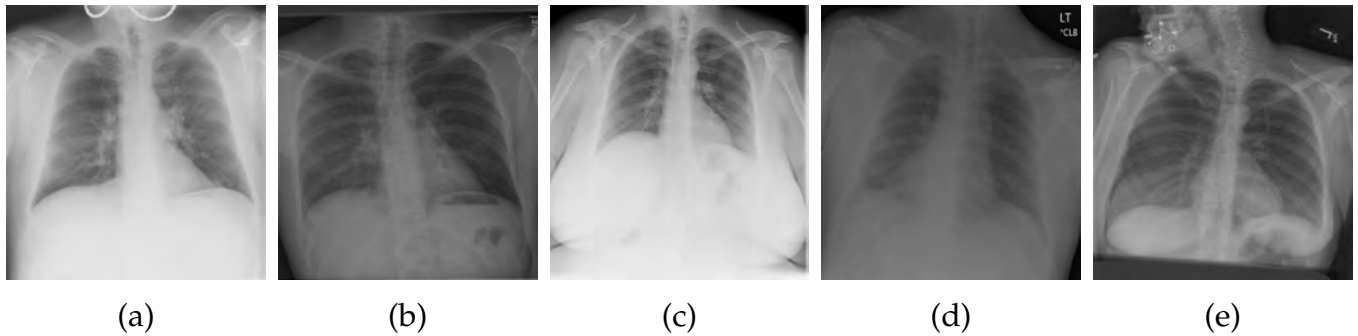


Fig. 2. Samples of chest radiographs in the order of increasing degree of rotation, from left to right (a – e). Radiologists do not consider sample (a) as rotated since there is a very small difference in the distance from the medial heads of the clavicles to the adjacent vertebral in the spinous processes (see Fig. 1).

drawback of the state-of-the-art methods since they require all pairs of ribs. Therefore, we propose a new method for computing the principal rib-orientation from both lungs. Missing a pair of ribs does not negatively affect the output of our method because the visible subset is sufficient to compute the principal rib-orientation. As a result, our method is more stable. Further, principal rib-orientation minimizes false positive detection caused by overlapping densities in a rotated radiograph. Our contributions¹ can be enumerated as follows.

1. We develop a novel generalized line histogram method to compute rib-orientations.
2. We apply this method as a decision making tool for rotation detection and quality control in acquisition of CXRs, particularly in remote rural areas during mass population automated screening.
3. Therefore, we overcome the limitations of highly sensitive clavicle detection methods since our method does not require any information about clavicles.

The remainder of this paper is organized as follows. We start with detailing our proposed method in Section 2. This includes lung segmentation, line seed filter (kernel) development, line histogram computation, and rotation decision. In Section 3, we evaluate the approach. We conclude the paper in Section 4 with a summary of our results.

2. Materials and method

2.1 Lung section segmentation

To effectively compute the rib-cage edge distribution, it is necessary to segment right and left lung sections from the whole image. Lung segmentation has a rich state-of-the-art literature. In this work, we apply our automatic algorithm which is based on graph-cut algorithm guided by a patient-specific atlas model [Candemir et al. \(2014\)](#). The system first builds a subset of

¹ The paper is a significant extension of the work presented in 27th IEEE Intl. Sympo. on Computer Based Medical Systems (CBMS) 2014, NY, USA [Santosh et al. \(2014\)](#).

atlases (which are expert delineations of lung boundaries of several patients) by choosing the most similar x-rays in terms of shape similarity of lungs. Then, it warps these selected atlases to the target CXR using a registration algorithm. We use the scale invariant feature transform (SIFT) flow (i.e., SIFT-flow) registration approach [Liu et al. \(n.d.\)](#), which computes the corresponding pixels of image pairs according to their SIFT feature similarity. The spatial difference between the corresponding pixels is used to warp the masks from training CXRs to build a lung model for the target CXR. The lung model and intensity information of the target CXR are combined by using the following objective function,

$$E(\mathbf{f}) = \alpha_d E_d(\mathbf{f}) + \alpha_s E_s(\mathbf{f}) + \alpha_m E_m(\mathbf{f}), \quad (1)$$

where

1. the data term E_d forces the segmentation to consider intensity information of the chest radiographs;
2. the smoothness term E_s ensures a smooth solution; and
3. the model term E_m guides the algorithm to produce segmentation results similar to the patient lung model.

Their corresponding scalar weights α_d , α_s and α_m are empirically determined. For more details about energy terms, we refer the reader to the work presented in [Candemir et al. \(2014\)](#). The final lung boundary is computed by solving the objective function with a graph cut energy minimization approach [Boykov et al. \(2001\)](#). [Fig. 3](#) shows output examples using our method, where the detected right and left lung sections are separately illustrated.

2.2 Generalized line histogram

The main idea in this section, is to approximate principal rib-orientations of both lung sections (as described in [Section 2.1](#)) for all possible angles: $[0, 180^\circ)$ in terms of line histograms by using line segment detector (via kernel convolution).

2.2.1 Kernels

To detect key lines from the image [Ye et al. \(2010\)](#), we design line seed filter kernels that are defined in a normal Gaussian distribution. We compute probability density functions (pdf) at each of the values in X using the normal distribution,

$$\mathbf{f}(x, \mu, \sigma) = \frac{1}{\sigma\sqrt{2\pi}} \exp\left(\frac{-(x - \mu)^2}{2\sigma^2}\right), \quad (2)$$

where $\sigma = 1$, $\mu = 0$ and X is a vector and its values are confined in the range $[-\sigma, \sigma]$. In the discrete case, a structuring element can be represented as a set of pixels on a grid, assuming the

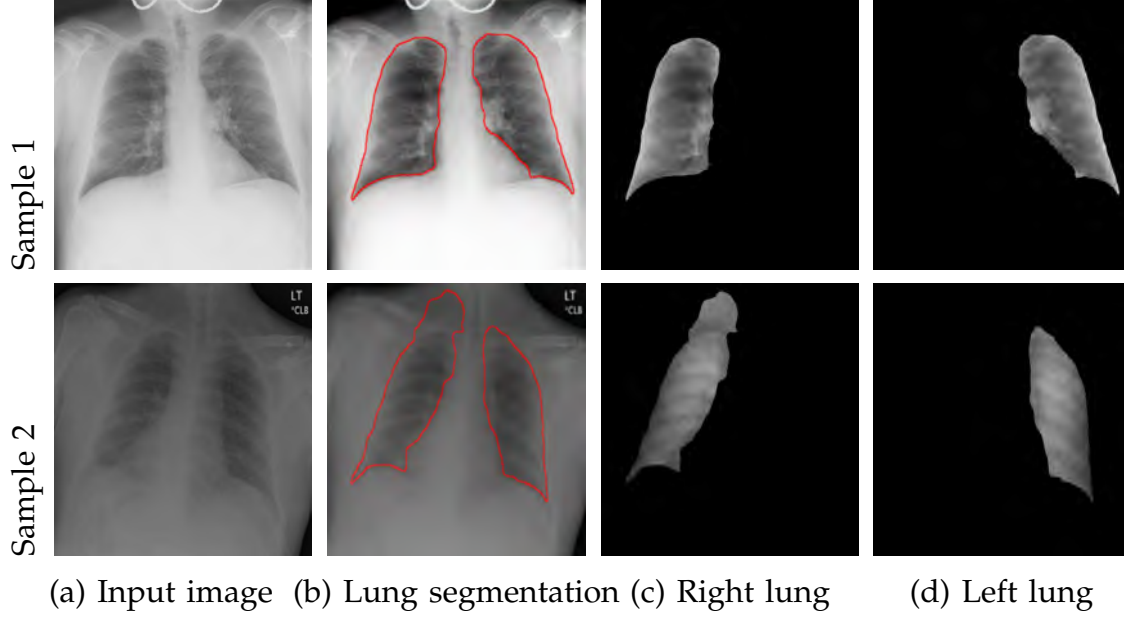


Fig. 3. Two examples showing the complete process of segmenting lung sections (right and left) using graph-cut algorithm.

values 1 if the pixel belongs to the structuring element or 0, otherwise [Hendriks & Vliet \(2003\)](#); [Serra \(1983\)](#). Based on this, we define a binary kernel representing a line of any particular length len and angle θ i.e., $\mathbf{f}('line', len, \theta)$. To generate a kernel that represents the 'bell-shaped' Gaussian distribution g , we perform an element-wise multiplication of the binary kernel with the values obtained from Eq. (2),

$$g = \mathbf{f}('line', len, \theta) \circ \mathbf{f}\left(\left[-\sigma : \frac{2\sigma}{len-1} : \sigma\right], \mu, \sigma\right). \quad (3)$$

The following example shows how kernels are made, for a particular angle θ and line length $len = 5$.

$$\begin{aligned} g \text{ at } 30^\circ &= \mathbf{f}('line', 5, 30) \circ \mathbf{f}\left(\left[-1 : \frac{2 \times 1}{5-1} : 1\right], 0, 1\right) \\ &= \begin{bmatrix} 0 & 0 & 0 & 1 & 1 \\ 0 & 0 & 1 & 0 & 0 \\ 1 & 1 & 0 & 0 & 0 \end{bmatrix} \circ [0.24 \ 0.35 \ 0.39 \ 0.35 \ 0.24] \\ &= \begin{bmatrix} 0 & 0 & 0 & 0.35 & 0.24 \\ 0 & 0 & 0.39 & 0 & 0 \\ 0.24 & 0.35 & 0 & 0 & 0 \end{bmatrix}. \end{aligned}$$

Note that the kernel matrix size depends on the length of the line. In order to avoid discretization errors and to get more precision, a larger matrix is required for small step angle differences in the range of $[0^\circ, 180^\circ)$. For example, in Fig. 4, kernels representing line filters in six different orientations are shown, where the kernel matrix size is 9×9 . While creating the kernel, its

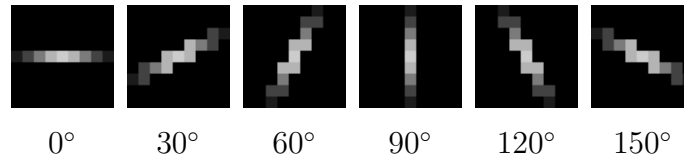


Fig. 4. Kernels representing linear structuring element i.e., line filters in six different orientations, defined in a 1D Gaussian distribution.

matrix size can be varied with the window size of the image, as well as with the application. For line drawing images as an example, the matrix size can be increased to exploit less but prominent lines. The larger the size of the kernel matrix, the fewer the number of lines.

We know that the Gaussian kernel is normalized to make the integral over the exponential function unity for every σ . As a consequence, the shape of the kernel remains the same, irrespective of σ . Further, the behavior of the kernel function is the same for all directions (isotropic). Gaussian kernel therefore, maximizes the filter response in the middle, which means that the line extraction addresses our key issue especially when it emphasizes continuous lines and curves (see Fig. 5). This makes Gaussian kernels different from binary. In a similar fashion, Hough transform [Hough \(1959\)](#) may not be useful to our application since it requires to fix several parameters like Hough peaks, line segment length and gap between the line segments. Additionally, like binary kernels, extracting continuous lines and curves is not trivial, which is our key issue.

Considering a set Θ of possible different orientations $\{\theta_k\}$ which are specified in the range $[0^\circ, 180^\circ)$, we have a set \mathcal{K} of kernels $\{g_k\}$,

$$\mathcal{K} = \{g_k\}_{k=1, \dots, K}, \text{ and } \theta_k = \frac{180^\circ}{\text{bin}_k} (k - 1). \quad (4)$$

The index k associated with kernel g determines the orientation angle i.e., θ_k . As an example, any orientation angle θ for different values of k and $\text{bin} = 6$ will be (cf. Fig. 4), $\theta_1 = 0^\circ$ when $k = 1, \dots, \theta_6 = 150^\circ$ when $k = 6$.

2.2.2 Line histogram via convolution

Given an edge image $\text{edg}I(m, n)$ of size $M \times N$, our idea is to perform convolution with the kernel g . Note that the edge image results from *Canny* edge detector after global histogram equalization. Convolution in general, can be expressed as $o(m, n) = g \otimes \text{edg}I$

$$o(m, n) = \sum_{i=1}^I \sum_{j=1}^J g(i, j) \text{edg}I(m - i, n - j). \quad (5)$$

For each pixel (m, n) in the image, the convolution output value $o(m, n)$ is calculated by translating the convolution mask to pixel (m, n) in the image, and then taking the weighted sum of the pixels in the neighbourhood about (m, n) , where the individual weights are the corresponding values in the convolution mask. Such a convolution produces prominent lines

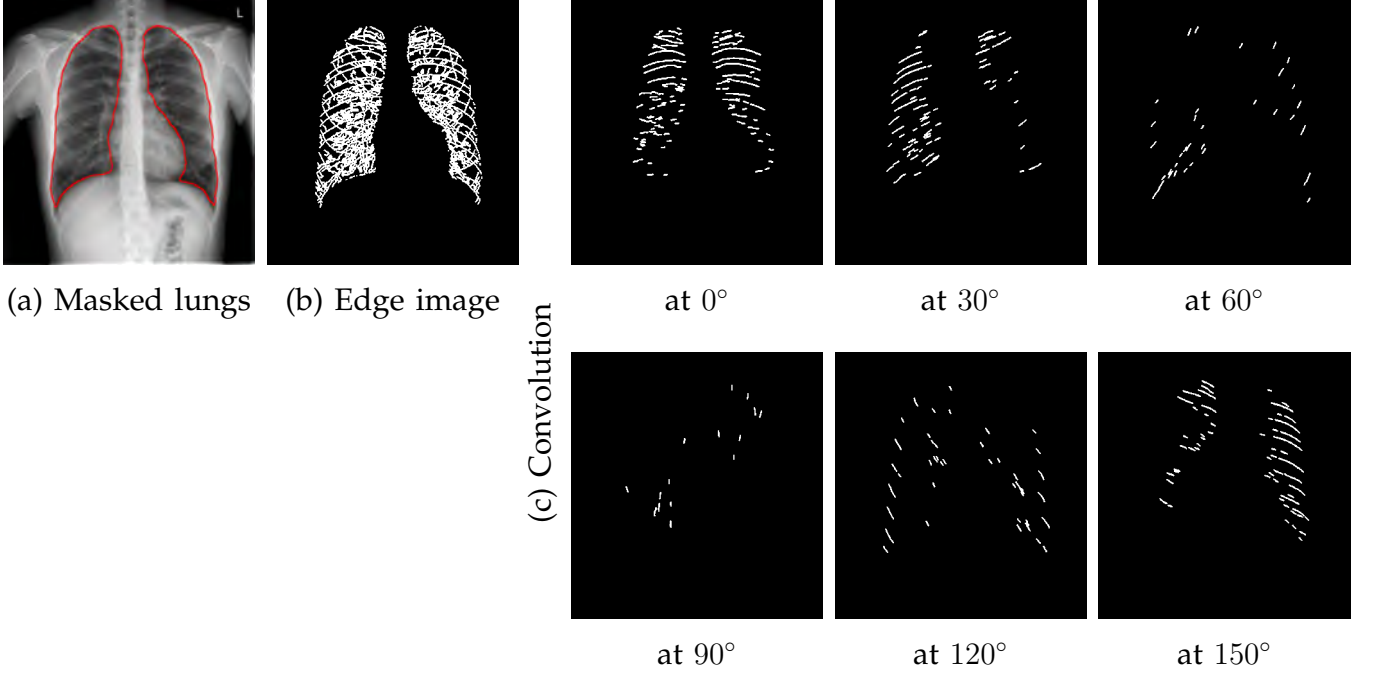


Fig. 5. Resulting lines after convolving the edge image with kernels in six different orientation angles (i.e., $0^\circ, 30^\circ, \dots, 150^\circ$), which are defined in 1D Gaussian distribution (cf. Fig. 4).

that are found in the lung section. Considering a complete set \mathcal{K} of kernels (defined in Eq. (4)), convolution will produce a complete set \mathcal{L} of lines ℓ_k ,

$$\mathcal{L} = \mathcal{K} \otimes \text{edg}I = \{\ell_k\}_{k=1, \dots, K}, \quad (6)$$

Such sets of lines result from the edges of rib cages and their neighbourhood pixels. Fig. 5 shows a few examples. In this illustration, different numbers and sizes of lines are extracted from six different kernels (based on the orientation angle i.e, $\theta = \{0^\circ, 30^\circ, \dots, 150^\circ\}$). Any ℓ_k can be represented by a tuple: total number of lines (noL) and total length of the lines (loL) i.e., $\ell = \langle noL, loL \rangle$. While computing histograms, either noL or loL can be used for any particular k . Since lengths of the lines vary from one line to another (Fig. 5), without loss of generality, it is interesting to take its length. Based on this, we can express it in terms of histogram h of lines in every convolution, designated by kernel g_k ,

$$\mathcal{H} = [\hbar_1, \dots, \hbar_k, \dots, \hbar_K] \text{ and } \hbar_k = \frac{1}{\max(h_k)} h_k, h_k = loL_k. \quad (7)$$

Overall, to compute a single histogram from any image, time complexity, T can be expressed as $T(K) = O(K)$, where K is the total number of kernels that are used for convolution.

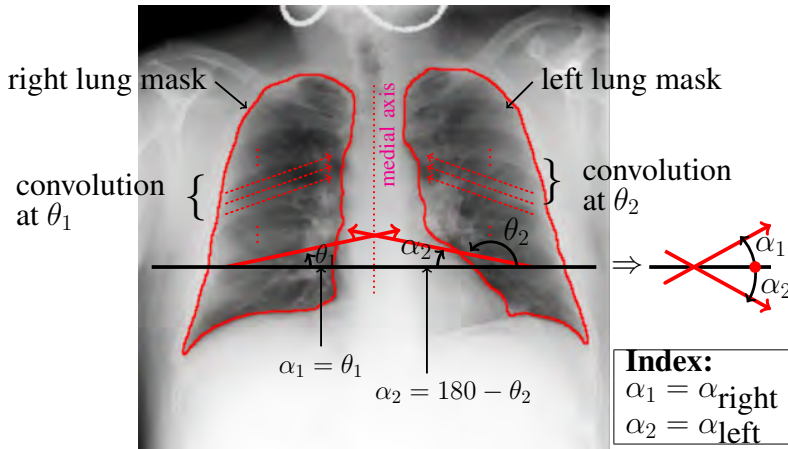


Fig. 6. An example (*cf.* sample 1 in Fig. 3), illustrating the way to compute chest radiograph rotation based on principal rib-orientations, by separately analyzing two lung sections: left and right.

2.3 Chest radiograph rotation

Following Eq. (7), principal chest rib-orientation can roughly be computed as, $\arg \max_k (\hat{h}_k)$, $k = 1, \dots, K$, where k determines at what angle the kernel has been used (*cf.* Eq. (4)). This means that the principal chest rib-orientation is the angle from which the maximum magnitude of line histogram results. Based on this, we set up a global decision process to decide whether the CXR is rotated.

Consider two lung sections: right and left, and kernels at several different θ values, the CXR is said to be upright if their orientation angle difference Δ is zero or negligible (see Fig. 6), $\Delta_{\alpha_{1,2}} = |\alpha_1 - \alpha_2| \approx 0$, where $\alpha_1 = \theta_1$ and $\alpha_2 = 180 - \theta_2$ respectively represent the principal rib-orientation angles from right and left lung sections. For practical use, since $\Delta_{\alpha_{1,2}} \neq 0$ (it is typically greater than zero), our decision relies on a small tolerance (tol.) to generate a binary response,

$$\text{decision} = \begin{cases} 1 \text{ (for rotation)} & \text{if } \Delta_{\alpha_{1,2}} \geq \Delta_{\alpha_{1,2}}^{\text{tol.}} \\ 0 \text{ (for non-rotation)} & \text{otherwise,} \end{cases} \quad (8)$$

where $\Delta_{\alpha_{1,2}}^{\text{tol.}}$ is designed based on the observations. In this work, we do not use the fixed tolerance value but, we tune it (within the provided range) to seek for the optimal performance. This will further be discussed in our experimental tests (Section 3.4).

3. Experiments

3.1 Datasets

We used two chest x-ray image datasets in our test: 1) Indiana (IN) and 2) Montgomery County (MC). The IN dataset is a large collection of over 4000 frontal radiographs covering a wide range of lung abnormalities. The images were collected from various hospitals affiliated with the Indiana University School of Medicine. From this dataset, we have selected rotated (50 samples) and a subset of 100 non-rotated samples. The MC dataset contains 138 frontal radiographs, where

several abnormal radiographs show manifestations of Tuberculosis and have abnormal lung shapes. The images were acquired within the tuberculosis control program of the Department of Health and Human Services of Montgomery County in Maryland, USA.

Both datasets² have been de-identified at source and are exempted by the respective IRBs at the source organizations and the National Institutes of Health (NIH).

3.2 Evaluation protocol

Since it is difficult to provide an accurate rotation angle for the expert, our evaluation protocol follows a qualitative response: rotated or non-rotated. In this testing protocol, the response returned from our algorithm is correct if it matches the expert’s response.

For evaluation, considering the whole dataset size B , we compute accuracy (acc.) of the algorithm’s response (AR) with respect to the expert’s response (ER) as,

$$\text{acc.} = \frac{\sum_{b=1}^B \text{AR}_b \wedge \text{ER}_b}{B}, \text{ and } \text{AR} \wedge \text{ER} = \begin{cases} 1 & \text{if } \text{AR} = \text{ER} \\ 0 & \text{otherwise,} \end{cases} \quad (9)$$

where responses ER and AR are binary sequences i.e., $\text{ER}_b, \text{AR}_b \in \{0, 1\}$.

3.3 Illustrative examples

Before reporting an overall performance of our algorithm, we first illustrate its operation through an example shown in Fig. 7. Here,

1. the solid horizontal line (in black) separates the line histograms from right and left lung sections;
2. the solid red lines represent the principal rib-orientation angles; and
3. different number of bins (quantization) are used to evaluate their effect on decision.

We remind the reader that the number of bins depends on the convolution angle interval (*cf.* Eq. (4)). In this example, for different number of bins viz. 6, 12 and 180, $\Delta_{\alpha_{1,2}}$ is always zero. These results show that the decision remains unchanged (i.e., up-right chest radiograph) even when number of bins vary. This, however, does not hold for all CXRs and $\Delta_{\alpha_{1,2}}$ can be bigger when using less number of bins. Furthermore, we observe that larger the number of bins, better the histogram’s precision. Therefore, we use angular steps of 1° for convolution, in all tests (Fig. 8).

² • The image datasets are available on request via <http://ceb.nlm.nih.gov>

• Indiana collection images may be viewed on NLM’s Openi system <http://openi.nlm.nih.gov>

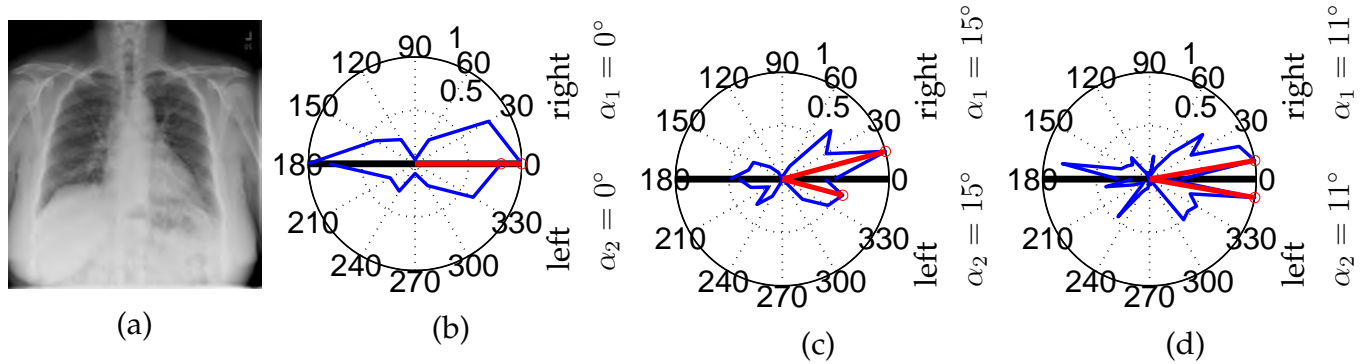


Fig. 7. An example showing line histograms from (a) a chest radiograph with three different number of bins: (b) 6 (at 30° see Fig. 5, for instance), (c) 12 (at 15°) and (d) 180 (at 1°), for making decisions. The sample, taken from the Indiana dataset has been decided to be fully up-right chest radiograph. In the example, rib-orientation angle difference $\Delta_{\alpha_{12}} = |11 - 11| = 0$ when $bin = 180$.

3.4 Results and analysis

Results from a range of tolerance values were obtained and the best result was selected. Separate tests have been made for rotated and non-rotated CXRs, and shown in Fig. 9. The results are based on the evaluation protocol described in Eq. (9) that follows decision criterion Eq. (8). In Fig. 9, the observation can be summarized as follows. With respect to the increasing tolerance value, starting from $\Delta_{\alpha_{1,2}}^{tol.} = 0$,

1. rejection of the rotated CXRs is gradually decreased; and
2. in contrast, there is a gradual increment of the acceptance of the non-rotated CXRs.

As shown in the reported results (Fig. 9), our aim is not to reject/accept 100% rotated/non-rotated CXRs. Therefore, we have studied their trade-off by maintaining the satisfactory performance, and the optimal results have been achieved in the range 5 – 14. This means that the algorithm cannot make a clear distinction between rotated and non-rotated samples outside that range. Further, since there always exists a small rib-orientation angle difference even from the up-right (non-rotated) CXRs, a smaller threshold $\Delta_{\alpha_{1,2}}^{tol.} = 5$, for instance can only accept approximately 42% up-right CXRs. But at the same time, it can reject approximately 95% of rotated CXRs. On the other hand, after $\Delta_{\alpha_{1,2}}^{tol.} = 10$, the rejection rate of rotated CXRs has been decreased to approximately 40% while accepting more than 92% up-right CXRs. This suggests that severely rotated CXRs are only detected when the threshold increases. For more clarity, Fig. 8 illustrates more examples, where our algorithm reports that all samples are rotated when $\Delta_{\alpha_{12}}^{tol.} = 5^\circ$ but, samples (a), (e) and (f) are not considered as rotated when $\Delta_{\alpha_{12}}^{tol.} = 10^\circ$.

For discussion, additional issues include 1) convolution angle-range, and 2) precision in rib-orientation. While mathematical formulation allows all possible angles from $0^\circ - 180^\circ$, practical implementations do not need to compute beyond 60° . This helps to reduce the execution time. Our algorithm does not precisely provide an individual rib-orientation, but an

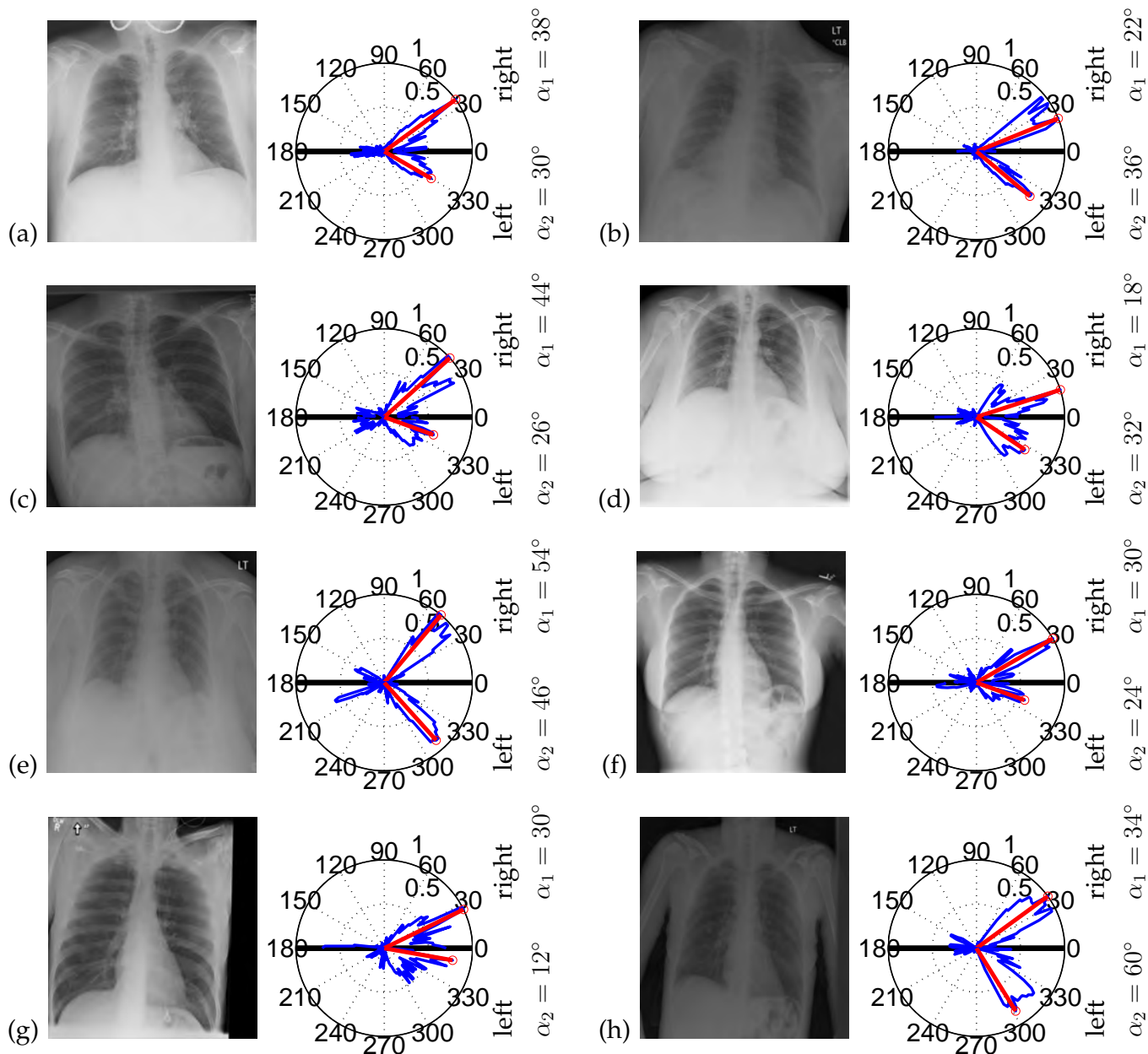


Fig. 8. Examples illustrating whether chest radiographs are rotated based on principal chest rib-orientation, when taking tolerance, $\Delta_{\alpha_{12}}^{tol} = 5^\circ$.

approximated single value for all ribs appearing in any particular lung section. This makes our computation is robust (*cf.* Fig. 8, sample (b)) even when some ribs are not visible or when there are false positives due to over-segmentation (*cf.* Fig. 3, sample (b)).

3.5 Performance with error-prone lung segmentation

Erroneous lung segmentation may not change the principal rib-orientation values as long as a large lung volume (approximately equal in both lung sections) remains within it. Additionally, to see how robust the algorithm is, another test has been made by using

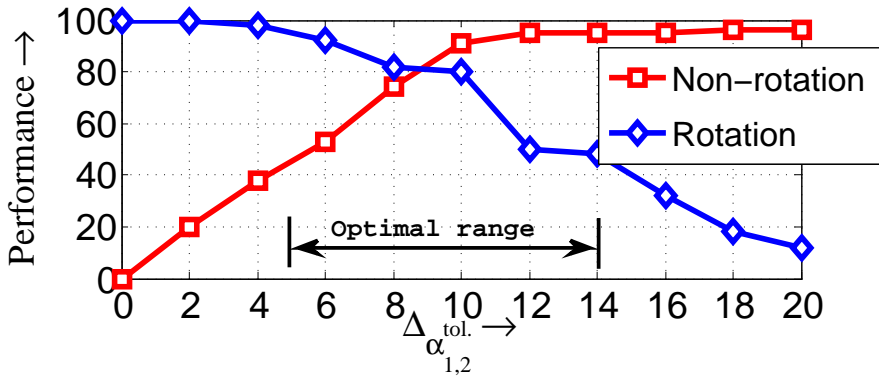


Fig. 9. Separate performances for rotated and non-rotated samples.

free-hand lung segmentation that can either over or under-segment (not limited to just a small leakage/elongation as shown in Fig. 3, sample 2). Like before, we start by generating line histogram illustrations for each segmentation (see Fig. 10). In case of under-segmentation, we observe that the rib-orientation angles are more precise in comparison to over-segmentation because curve-like rib cage regions are avoided. Therefore, in our test, under-segmentation is found to be effective. But, the algorithm’s decision is highly influenced if we apply both over and under-segmentation in a single CXR. Therefore, no such samples have been used in the test.

To determine the interest and to evaluate the robustness of the free-hand segmentation, comparison has been made with automatic lung segmentation, and shown in Fig. 11, where the curve (in blue) is the average performance from Fig. 9. The comparison shows similar behavior.

4. Summary and future work

In this paper, we have presented a method for detecting rotation in frontal CXRs by developing a generalized line histogram based rib-orientation detector. The method uses a line seed filter kernel to convolve with an edge image that produces a set of lines in several different possible directions, ranging from 0° to 180° . The angle for which the magnitude of the histogram is maximum is the principal rib-orientation angle. Considering both (left and right) lung sections, from our experimental tests, we have observed that the proposed method can distinguish

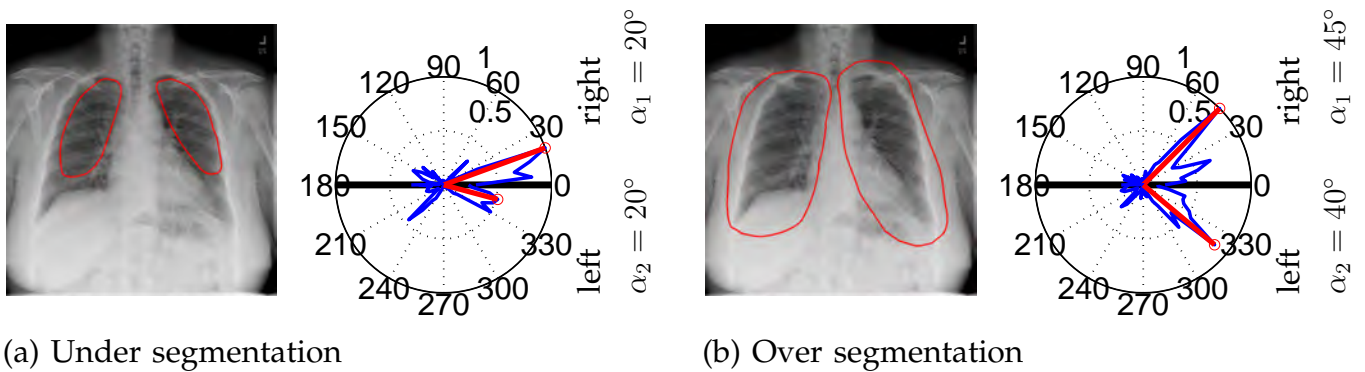
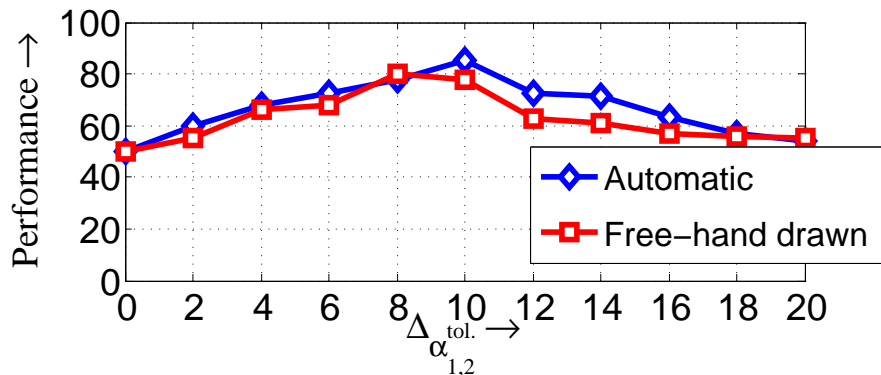


Fig. 10. Resulting line histograms based on the corresponding free-hand lung segmentation: (a) under and (b) over segmentation.

Fig. 11. Performance comparison (in average, including both rotated and non-rotated samples) between automatic and free-hand lung segmentation.



severely rotated CXRs from non-rotated ones, and achieved a maximum overall accuracy of 89.1%.

The proposed method, on the other hand, does not extract sufficient line segments from those CXRs having lung sections where ribs are not clearly visible due to pleural effusion, for instance and other diseases such as pneumonia. Similarly, line histograms are affected when anterior ribs are pronounced than posterior ones, which is still a rare case. Fig. 12 shows some examples. Furthermore, as discussed in Section 3.5, the algorithm fails when over-segmentation has been made in one lung section and under-segmentation in another. In such context, decisions are affected from non-rotated CXRs but they remain valid for rotated CXRs.

As future work, we aim to integrate texture-based filtering techniques for pre-processing CXRs to minimize problems due to intensity variations Zuo et al. (2013). Such a feature (1D line histogram) can also be useful for detecting abnormalities via symmetric similarity. Computing lung symmetry (reflective symmetry) based on the rib distribution is another plan in order to detect abnormalities in CXRs. For an immediate understanding, in Fig. 7, the line histograms can help to estimate the reflective symmetric similarity between right and left lung sections.

Acknowledgements

This research was supported by the Intramural Research Program of the National Institutes of Health (NIH), National Library of Medicine (NLM), and Lister Hill National Center for

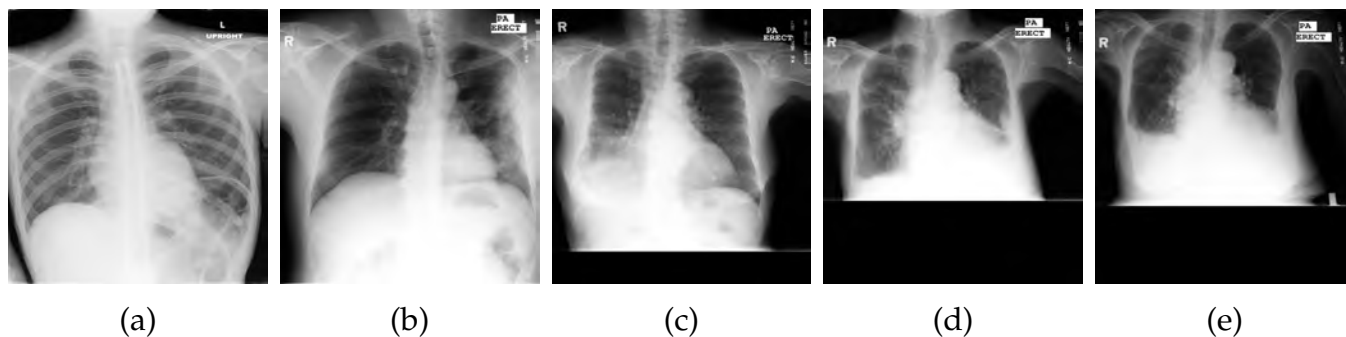


Fig. 12. Samples where the algorithm has failed to make a correct decision when (a) anterior ribs look more prominent than posterior ones and (b-e) ribs are not visible in any lung section.

Biomedical Communications (LHNCBC). The authors would like to thank the NIH Fellows Editorial Board for their editorial assistance.

5. References

- Bongard, F., Sue, D. & Vintch, J. (2008). *Current Diagnosis and Treatment Critical Care*, McGraw-Hill Education.
- Boykov, Y., Veksler, O. & Zabih, R. (2001). Fast approximate energy minimization via graph cuts, *IEEE Trans. Pattern Anal. Mach. Intell.* **23**(11): 1222–1239.
- Candemir, S., Jaeger, S., Musco, J., Xue, Z., Karargyris, A., Antani, S., Thoma, G. & Palaniappan, K. (2014). Lung segmentation in chest radiographs using anatomical atlases with non-rigid registration, *IEEE Trans. on Medical Imaging* **33**(2): 577–590.
- Corne, J. & Pointon, K. (2010). *Chest X-Ray Made Easy*, Elsevier Health Sciences.
- de Souza, P. (1983). Automatic rib detection in chest radiographs., *Computer Vision, Graphics, and Image Processing* **23**(2): 129–161.
- Folio, L. (2010). *Combat Radiology: Diagnostic Imaging of Blast and Ballistic Injuries*, Springer.
- Folio, L. (2012). *Chest Imaging: An Algorithmic Approach to Learning*, Springer.
- Folio, L. (2014). Interpretive approach and reporting the intensive care bedside chest x-ray, *Journal of American Osteopathic College of Radiology* **3**(2): 12–20.
- Grivas, T. B., Burwell, R. G., Purdue, M., Webb, J. K. & Moulton, A. (1992). Segmental patterns of rib-vertebra angles in chest radiographs of children: Changes related to rib level, age, sex, side and significance for scoliosis, *Clinical Anatomy* **5**(4): 272–288.
- Hendriks, C. & Vliet, L. (2003). Discrete morphology with line structuring elements, in N. Petkov & M. Westenberg (eds), *Int. Conf. on Computer Anal. of Images and Patterns*, Vol. 2756 of *Lecture Notes in Computer Science*, Springer Berlin Heidelberg, pp. 722–729.
- Herring, W. (2011). *Learning Radiology: Recognizing the Basics*, Elsevier Health Sciences.
- Horváth, G., Orbán, G., Horváth, A., Simkó, G., Pataki, B., Máday, P., Juhász, S. & Horváth, A. (2009). A cad system for screening x-ray chest radiography, in O. D'Áussel & W. Schlegel (eds), *World Congress on Medical Phys. and Biomedical Eng.*, Vol. 25/5, Springer Berlin Heidelberg, pp. 210–213.
- Hough, P. (1959). Machine Analysis Of Bubble Chamber Pictures, *High Energy Accelerators and Instrumentation*, pp. 554–558.
- Iakovidis, D. K., Savelonas, M. A. & Papamichalis, G. (2009). Robust model-based detection of the lung field boundaries in portable chest radiographs supported by selective thresholding, *Meas. Sci. Technol* **20**(10).
- Jaeger, S., Karargyris, A., Candemir, S., Folio, L., Siegelman, J., Callaghan, F., Xue, Z., Palaniappan, K., Singh, R., Antani, S., Thoma, G., Wang, Y.-X., Lu, P.-X. & McDonald, C. J. (2014). Automatic tuberculosis screening using chest radiographs, *IEEE Trans. on Medical Imaging (to appear)*.
- Jaeger, S., Karargyris, A., Candemir, S., Siegelman, J., Folio, L., Antani, S., Thoma, G. & McDonald, C. J. (2013). Automatic screening for tuberculosis in chest radiographs: a

- survey, *Quant. Imaging in Medicine and Surgery* **3**(2).
- Karargyris, A., Antani, S. & Thoma, G. (2011). Segmenting anatomy in chest x-rays for tuberculosis screening, *Int. Conf. of the IEEE Eng. in Medi. and Bio. Soc.*, pp. 7779–7782.
- Liu, C., Yuen, J. & Torrallba, A. (n.d.). SIFT flow: Dense correspondence across different scenes and its applications., *IEEE Trans. Pattern Anal. Mach. Intell.* **33**(5): 978–994.
- Matsuo, Y., Shimizu, A. & Kobatake, H. (2005). An interval change detection method for two chest x-ray images with different rotation angles of the human body and its performance evaluation, *Systems and Computers in Japan* **36**(10): 30–42.
- Mehta, M. H. (1972). The rib-vertebra angle in the early diagnosis between resolving and progressive infantile scoliosis, *Journal of Bone and Joint Surgery - British Volume* **54**(2): 230–243.
- Puddy, E. & Hill, C. (2007). Interpretation of the chest radiograph, *Continuing Education in Anaesthesia, Critical Care & Pain* **7**(3): 71–75.
- Santosh, K. C., Candemir, S., Jaeger, S., Folio, L., Karargyris, A., Antani, S. & Thoma, G. (2014). Rotation detection in chest radiographs based on generalized line histogram of rib-orientations, *IEEE, International Symposium on Computer-Based Medical Systems*, pp. 138–142.
- Serra, J. (1983). *Image Analysis and Mathematical Morphology*, Academic Press, Inc., Orlando, FL, USA.
- Suzuki, K., Abe, H., MacMahon, H. & Doi, K. (2006). Image-processing technique for suppressing ribs in chest radiographs by means of massive training artificial neural network (mtann), *IEEE Trans. on Medical Imaging* **25**(4): 406–416.
- van Ginneken, B., Stegmann, M. B. & Loog, M. (2006). Segmentation of anatomical structures in chest radiographs using supervised methods: a comparative study on a public database, *Medical Image Analysis* **10**(1): 19 – 40.
- Wechsler, H. (1977). *Automatic detection of rib contours in chest radiographs: an application of image processing techniques in medical diagnosis*, Interdisciplinary systems research, Birkhäuser.
- Ye, Z., Hongsong, Q. & Yanjie, W. (2010). Scene matching based on directional keylines and polar transform, *IEEE International Conference on Signal Processing (ICSP)*, pp. 857–860.
- Zuo, W., Zhang, L., Song, C. & Zhang, D. (2013). Texture enhanced image denoising via gradient histogram preservation, *IEEE Conf. on Computer Vision and Pattern Recogn.*, pp. 1203–1210.

Authors' biography

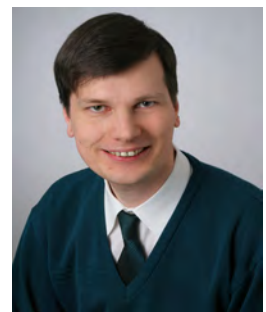
Dr. K. C. Santosh is currently a research fellow at the LHNBC, an R&D division of the U.S. National Library of Medicine (NLM), National Institutes of Health (NIH), USA. Before this, K. C. worked as a postdoctoral research scientist at the LORIA research centre, Université de Lorraine and ITESOFT, France. K. C. earned his Ph.D. in Computer Science from INRIA Nancy Grand Est, Université de Lorraine, France in 2011 under the FP-6 European project (and INRIA-CORDI research grant), Master of Science diploma in Information Technology by research and thesis from the School of ICT, SIIT, Thammasat University, Thailand in 2007 under the ADB-JSP, and Bachelor of Engineering in Electronics and Communication from Pokhara University, Nepal, in 2003, under a merit scholarship. His research interests include document image analysis, document information content exploitation, biometrics (such as face and shoeprint) and biomedical image analysis. Dr. K.C. is a part of chest x-ray screening project for detecting Tuberculosis, at the NLM.



Dr. Sema Candemir received her doctorate degree in 2011, in computer engineering from Gebze Institute of Technology, Turkey. She worked as a postdoctoral researcher at University of Missouri-Columbia, where she collaborated with Air Force Research Laboratory and Kitware Company towards robust target tracking in wide area imagery. She is currently a postdoctoral researcher in National Library of Medicine, in Communication Engineering Branch, and a member of the chest X-ray screening project team. Her research interests are computer vision and image processing.



Dr. Stefan Jaeger is a research fellow at the Lister Hill National Center for Biomedical Communications at the United States National Library of Medicine (NLM), part of the National Institutes of Health (NIH). He received his diploma from University of Kaiserslautern (German Research Center for Artificial Intelligence) and his PhD from University of Freiburg, Germany, both in computer science. Dr. Jaeger has an international research background, in academia as well as in industry. He has held, among others, research positions at Chinese Academy of Sciences, University of Maryland, Tokyo University of Agri. & Tech., University of Karlsruhe, and Daimler. His research interests include biomedical imaging, pattern recognition, machine learning, and theoretical medicine. He has published actively in these areas, receiving several best paper awards and nominations for his work. Most recently, he has implemented methods for cell classification and tracking. At NIH, Dr. Jaeger is currently developing a screening system



for detecting tuberculosis in chest x-rays, as part of an initiative to improve tuberculosis detection in developing countries.

Dr. Alexandros Karargyris graduated from National Technological University of Athens, Greece with a Masters degree in Electrical Engineering and Computer Engineering in 2006. In 2010 he earned his PhD in Computer Science from Wright State University. Since 2010 he has been with the National Library of Medicine of National Institutes of Health in Bethesda MD working for a multinational consortium to help with the design of a cost-effective system for tuberculosis detection at low-resourced areas. His current research areas are medical imaging and machine learning. In the past he has been a holder of NSF and Ohio Board of Regents (OBR) scholarships.



Dr. Les Folio is a radiologist in Body Imaging and lead radiologist for Computed Tomography at the National Institutes of Health (NIH) in Bethesda, MD. He is also a Clinical Professor (adjunct), George Washington University Hospital. Dr. Folio has four medical specialties; in addition to radiology, he trained and practiced in Occupational, Preventive and Aerospace Medicine. He is a Fellow of the American Osteopathic College of Radiology.



Dr. Folio retired from the Air Force as a Colonel in the summer of 2009. His latest assignments included Walter Reed Army Medical Center, Uniformed Services University and the Pentagon. While in the military, he deployed to hospitals in the Middle East including Iraq. His book "Combat Radiology Imaging of Blast and Ballistic Injuries" is based on his military experiences while treating wounded warriors. Dr. Folio has chaired (and presented) several trauma conferences both nationally and internationally. He has over 60 publications in peer reviewed journals and six books with his latest book titled "Chest Imaging, an Algorithmic Approach" was published in November 2011.

Dr. Sameer Antani is a Staff Scientist with the National Library of Medicine part of the National Institutes of Health. He leads R&D projects in biomedical image processing, multimodal information retrieval, machine learning, and mobile health apps, He earned a B.E. from the University of Pune, India, in Computer Engineering, and M.Eng. and Ph.D. from the Pennsylvania State University in Computer Science and Engineering. Dr. Antani is a Senior Member of the SPIE, and a member of the IEEE, and its



Computer Society. He serves on the editorial board of the IEEE Journal of Biomedical and Health Informatics, in addition to other leadership roles.

Dr. George R. Thoma is Chief of the Communications Engineering Branch of the Lister Hill National Center for Biomedical Communications, a research and development division of the U.S. National Library of Medicine at the National Institutes of Health. In this capacity, he directs intramural R&D in mission-critical projects such as the automated extraction of bibliographic data from medical articles to populate the MEDLINE database, digital preservation, animated virtual books, a system to aid family reunification in mass disaster events, and multimedia-rich interactive publications. These projects rely on techniques from document image analysis, biomedical image processing and machine learning, and appear at archive.nlm.nih.gov. He earned a B.S. from Swarthmore College, and the M.S. and Ph.D. from the University of Pennsylvania, all in Electrical Engineering. Dr. Thoma is a Fellow of the SPIE, the International Society for Optical Engineering.

